In situ damage mechanisms investigation of PA66/GF30 composite: Effect of relative humidity

M.F. Arif [a], F. Meraghni [a,*], Y. Chemisky [a], N. Despringre [a], G. Robert [b]

A B S T R A C T

Damage mechanisms of injection molded polyamide-66/short glass fiber 30 wt% composite (PA66/GF30) were analyzed using in situ SEM mechanical tests on specimens conditioned under three relative humidity contents (RH = 0%, 50% and 100%). The validity of these in situ analyses was confirmed by X-ray micro-computed tomography (μCT) observations on tensile loaded specimens. Experimental results demonstrated that relative humidity (RH) conditions influence strongly the damage level and damage mechanisms. Indeed, for specimen with RH = 0%, damage initiation occurs at significantly higher load level than those in RH = 50% and RH = 100% specimens. The higher relative humidity condition also results in higher damage level. Damage chronologies have been proposed as damage initiation in the form of fiber–matrix debonding occurs at fiber ends and more generally at locations where fibers are close to each other due to the generation of local stress concentration (for all studied RH contents), and first fiber breakages occur (RH = 0%). These debonded zones further propagate through fiber–matrix interface (for all studied RH contents), and new fiber breakages develop (RH = 0%). At high relative flexural stress, matrix microcracks appear and grow regardless the RH contents. For RH = 100%, these microcracks are also accompanied by many matrix deformation bands. Subsequently, they lead to the damage accumulation and then to the final failure.

1. Introduction

Polyamide/short glass fiber composite materials (PA/GF) are widely used in automotive industry due to their high strength-to-weight ratio and the ability of injection molding to produce affordable geometrically complex parts. One of the challenges of designing components made of PA/GF arises from the ability of polyamide matrix to absorb water. The amount of absorbed water, depending on the environmental conditions such as temperature and relative humidity, highly influences the physical, thermal and mechanical properties of the composite.

In polyamide thermoplastics, the polar amide groups generate strong interactions in the crystalline and amorphous phases, with hydrogen bonds being established between neighboring molecules. Despite their strong interactions, these hydrogen bonds exhibit a disadvantage as they can lead to water absorption. The water molecules in the amorphous phase can interact with the amide groups which consequently weaken the preexisting inter-chain hydrogen bonds. Eventually, this can increase the chains mobility of the polyamide (plasticization effect). Meanwhile, swelling effect can also occur since a certain amount of water is absorbed by the polyamide [1–4]. The plasticization highly impacts the polyamide properties as it reduces its glass transition temperature [5]. It also influences the mechanical properties of the polyamide matrix such as a reduction of the strength and modulus while increasing the ductility [6]. The swelling effect of polyamide matrix can induce a mismatched fiber–matrix volume expansion and thus creating a residual stress which in turn can reduce the fiber–matrix interfacial properties [7,8].

Damage characterization of PA/GF has been studied by several authors. However, although the influence of environmental conditions, mainly the water uptake, on the physical and mechanical properties have been understood, no studies were analyzing the effect of relative humidity on the damage mechanisms and their effects on the overall mechanical behavior of PA/GF. The main paper focusing on in situ damage investigation of PA/GF is the work by Sato et al. [9] which reported that the damage starts from fiber ends and further propagates along the fiber–matrix interface. Horst and Spoormaker [10,11] and Barbouchi et al. [12] studied the fatigue fracture surface of PA/GF and similar damage mechanisms as those proposed by Sato et al. [9] for static loading were observed. Mouhmid et al. [13] used acoustic emission and scanning electron microscopy (SEM) techniques to investigate different types of

damage in PA/GF. They reported that the damage mechanisms in PA/GF are characterized by matrix plasticization and microcracks, fiber pull out and fracture. X-ray micro-computed tomography (μCT) technique has been used to investigate damage mechanisms in various composite materials [14–18]. Thanks to its inherent 3D analysis capabilities, the damage mechanisms can be identified and quantified in the bulk material, though usually careful data treatments are needed such as to resolve the lower resolution of μCT voxel as compared to the damage size and the presence of artifacts [18–20]. All these previous works did not focus on the effects of relative humidity on the damage initiation and accumulation in reinforced thermoplastics. Therefore, investigating the effects of relative humidity can be considered as important since it can change the matrix and interfacial properties of the composite and accordingly it may influence their damage mechanisms.

The study of the physical aspects of damage mechanisms is important to develop a more reliable and accurate modeling of their effects towards a reliable prediction of the overall mechanical behavior of the composite. A challenging topic in short fiber reinforced thermoplastics would be to develop models integrating the damage mechanisms, their initiation and kinetics. However, an extensive bibliographic review on reinforced thermoplastics shows that no modeling approach proposes unified consideration of the whole factors affecting the overall behavior and strength, i.e. composite microstructure, damage mechanisms, polymer rheology, hygrothermal conditions, loading level and paths, etc. [21–26].

In this work, in situ SEM tests were performed to identify the damage mechanisms of injection molded polyamide-66/short glass fiber 30 wt% composite (PA66/GF30) on specimens that have been conditioned at 23 °C under three different relative humidity conditions: RH = 0%, 50% and 100%. The RH = 0%, 50% and 100% specimens represent approximately conditions where the composites are respectively in glassy, glass transition and rubbery states, according to the RH effect on the glass transition temperature [26,27]. For a confirmation purpose, the results of μCT on the RH = 0% and 50% specimens will be presented. The results provided by the in situ SEM tests and μCT under different environmental conditions shall help to better understand the damage mechanisms of PA66/GF30 and then to implement them in a reliable modeling approach to predict the overall behavior of the composite.

Section 2 presents the material description and describes the procedure of sample preparation. In Section 3, the experimental procedures of in situ SEM tests and μCT are detailed. In Section 4, the results are discussed for each specimen conditioned under various relative humidity. The damage mechanisms are identified and compared in each case. Conclusions provide a damage scenario that considers the effect of the relative humidity content for the PA66/GF30 composite material.

2. Material description and sample preparation

2.1. PA66/GF30 and process induced microstructure description

The material for this study is Technyl® A218V30, a commercial grade of PA66/GF30 supplied by Solvay Engineering Plastics-France. The material was prepared by compounding the polyamide pellets and glass fibers in a twin-screw extruder. Subsequently, the PA66/GF30 compound was transferred into an injection molding machine, resulting in a 3.2 mm thickness of rectangular plate. The polished surfaces of the top and the through-thickness zones of machined specimen from the central region of injected plate were observed by scanning electron microscope (SEM). As described in Fig. 1, this material has a specific microstructure characterized by a well-defined skin–shell–core layer formation. This microstructure was only noticed through the thickness of the material and no microstructure heterogeneity was found through the width and length of the rectangular plate. This type of formation has been frequently observed in a thin plate structure of thermoplastic composites manufactured by injection molding process [28–30].

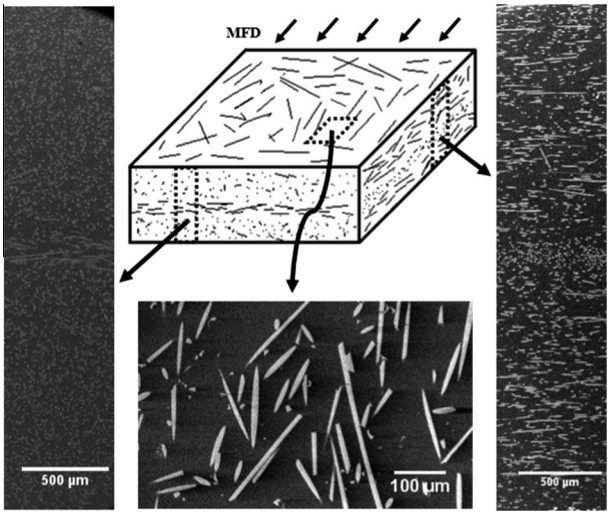

Fig. 1. Skin–shell–core microstructure formation developed through the thickness of the composite due to the injection molding process.

The skin layers, the upper and lower specimen surfaces, are randomly oriented and they represent about 5% of the plate thickness. The shell layers, with preferential orientation longitudinal with respect to the mold flow direction (MFD), are the most dominant layers. Indeed, they represent about 90% of the plate thickness. The core layer fills up to 5% of the plate thickness and mostly fibers in this layer are oriented perpendicular to MFD (Fig. 1).

Basically, the injection process induced fibers distribution is commonly established through the open literature [28–30]. In fact, fibers are globally oriented parallel to the shear flow direction. This can be explained by the well-known velocity profile and its related shear flow distribution in a molded plate. The latter is the main flow component during injection process. It has a maximum value close to the mold wall, whereas the shear flow vanishes in the core zone. This leads fibers oriented longitudinal to MFD at the shell layers and oriented perpendicular to MFD at the core layer. A thin random skin layers can be formed due to the polymer melt that is in direct contact with the relatively cold temperature of the mold wall and thus fibers freeze without any preferential orientations.

2.2. Preparation of specimens

Specimens for in situ characterization were machined in longitudinal (parallel) direction to MFD from the rectangular plate produced by injection molding. The specimens were 45 mm long with 10 mm width and a thickness of 3.2 mm. The conditioning of the specimens have led to equilibrium moisture content corresponding to three different relative humidity conditions, i.e. RH = 0%, 50% and 100%. It is worth noting that the water uptake does not affect the composite microstructure. Accordingly, the material microstructure described in Section 2.1 is thus valid for the three studied RH conditions.

An accelerated conditioning method was used to obtain an equilibrium water uptake equivalent to the RH = 0%, RH = 50% and RH = 100%, at 23 °C. The sample conditioned under RH = 0% was first polished then conditioned under vacuum oven at 80 °C

for 15 h to repel the water and ensure zero moisture content in the whole sample. The RH = 50% specimen was first polished and then prepared according to ISO 1110 standard, as the specimen has been conditioned inside a weathering chamber at 70 °C and RH = 62% until a constant weight was obtained. The procedure was continued by one week specimen conditioning at 23 °C, RH = 50% to make homogenous and equilibrium water concentrations in the whole sample. The specimen with RH = 100% was obtained by immersing the sample in boiling water for 35 h, followed by sample polishing and then water immersion at room temperature for one week. Subsequently, all the dry and humid specimens were sputtered with a thin layer of gold prior to in situ SEM testing and observations. It is worth noting that the plasticization process governed by the water uptake of the polyamide is a reversible process. The water content of the sample can be thus reduced or increased depending on the RH condition. Therefore, ensuring the material to reach equilibrium water content according to the designated relative humidity condition is important.

3. Microscopic damage characterizations

3.1. In situ SEM bending tests

In situ observations were performed by subjecting the specimens into a flexural load using a three-point bending micro-machine, with a span length of 27 mm, positioned inside a large SEM chamber (JEOL JSM-7001F). The crosshead speed of the contact central-point was set up to 400 μm/min. The displacement of the crosshead speed was interrupted in fixed positions to allow the in situ observation and images acquisition. To reduce the relaxation effect in the material, the observation time while maintaining the load was limited to 3 min. The observation area corresponded to the thickness surface of the composite with a particular emphasize at the outermost tensile region of the specimen, notably at the shell layer of the specimen. The three-point bending loading condition leads to a maximum stress at the outermost tensile region, which has an advantage to narrow down the observation to the zone where the maximum damage can be expected. It must be emphasized that since the main objective of the current work is to focus on the damage mechanisms investigation, the in situ SEM observations carried out at very local and high magnification are hence required. Therefore local fiber configurations such as fibers close to each other, fiber orientation perpendicular and transverse to the macroscopic stress direction were frequently observed regardless to the fact that the in situ observations were mainly performed on the shell layer where average fiber orientation is perpendicular to the macroscopic stress direction.

3.2. X-ray micro-computed tomography (μCT) observations

For a confirmation purpose of the in situ SEM observations, μCT technique was employed to investigate the damage mechanisms of PA66/GF30 specimens conditioned at RH = 0% and 50% that have been subjected to tensile loading. Dog-bone tensile specimens were machined in longitudinal direction to MFD from the PA66/GF30 rectangular plate. The virgin non-tested sample with RH = 0% extracted from the rectangular plate was also carried out for a comparison with the tensile loaded specimens. The μCT experiments were performed at beam line ID19 of European Synchrotron Radiation Facility (ESRF) in Grenoble, France [31]. The voxel resolutions achieved by the ID19 system were 0.7 and 1.4 μm. Both resolutions provided qualitatively relevant physical information. The μCT experiments were performed on samples with the size of $2 \times 2 \times 3.2\ mm^3$. The tensile loaded μCT samples were extracted from the specimens that have been tensile loaded up to failure. The cutting locations of the samples were far from the fracture surface in order to avoid fast crack propagation effect due to the failure. It is expected that ultimate damage mechanisms can be found at this maximum load.

4. Experimental results and discussion

4.1. Overall mechanical properties

Fig. 2 shows the normalized load – displacement responses of the in situ SEM three-point bending tests of PA66/GF30 specimens conditioned at various RH conditions. For each specimen, the relative ultimate loads before failure were recorded. Flexural strength (σ_f) was defined, for each RH content, as the maximum flexural stress in the specimen at the ultimate load according to ISO 178 standard. Relative flexural stress was defined to be the ratio of flexural stress in the area of observation with respect to the flexural strength. As described in Fig. 2, the RH content highly influences the mechanical properties of PA66/GF30. Flexural strength and stiffness of PA66/GF30 decreases with the increase of RH. The noticeable differences on the strength and modulus of PA66/GF30 by variation of RH are assumed to be due to damage and plasticization effect. Indeed, the RH = 0%, 50% and 100% specimens represent the conditions where the composites are respectively in glassy ($T_g > T_{room}$), glass transition ($T_g \approx T_{room}$) and rubbery states ($T_g < T_{room}$) [26,27]. Strain to failure in RH = 50% and 100% specimens are higher than that in RH = 0% specimen, whereas no significant difference is observed between the strain to failure at RH = 50% and 100% specimens. While the increase of strain to failure due to higher RH is noticeable for pure polyamide 66, this phenomenon is not strongly marked for fiber reinforced composite material [32].

4.2. Experimental results on relative humidity effects

4.2.1. SEM observations and analysis

(a) RH = 0% specimen: Fig. 3 shows typical microstructure observed on the thickness surface specimen before applying any load. For the three studied RH conditions (RH = 0%, RH = 50% and RH = 100%), the local views, corresponding respectively to Fig. 3a–c confirm that no indication of initial damage is observed regardless of the RH conditions.

While the load increases, the damage on RH = 0% specimen starts to be noticeable at around 33% σ_f. Damage initiations in the form of interfacial debonding at fiber end and fiber breakages are observed (Fig. 4a). It can be noticed in Fig. 4b that the matrix

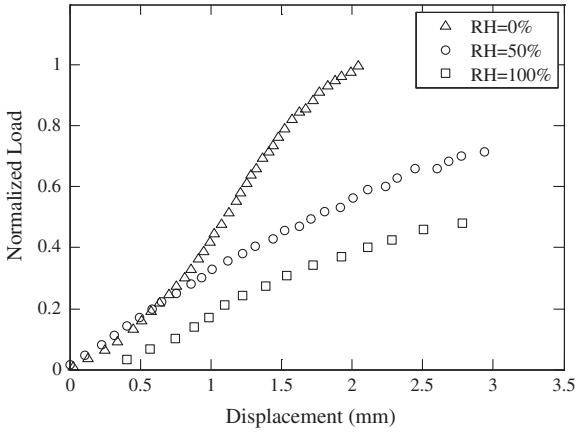

Fig. 2. Normalized load vs. displacement curve of PA66/GF30 specimens with variation of relative humidity.

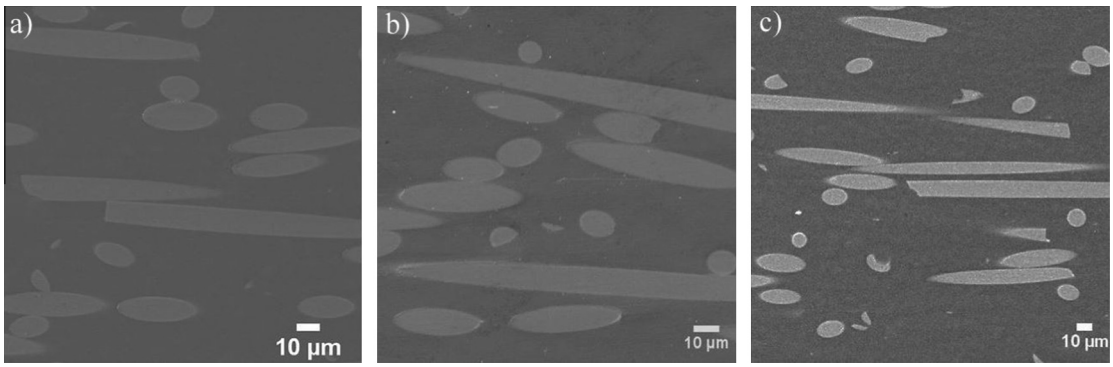

Fig. 3. Local views of virgin surface (at zero level stress) of PA66/GF30 specimen for the three RH contents: (a) RH = 0%, (b) RH = 50% and (c) RH = 100%. One can notice that no indication of initial damage is detected regardless of the RH conditions.

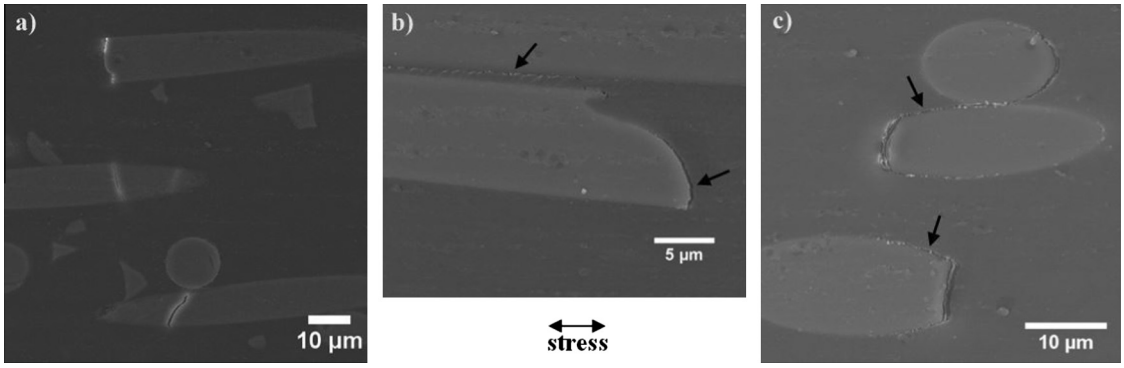

Fig. 4. PA66/GF30, RH = 0% specimen, (a) damage at fiber end and fiber breakages at 33% σ_f, (b) damage at fiber end and high plastic deformation between two adjacent fibers at 48% σ_f, and (c) damage propagation along fiber–matrix interface at 85% σ_f.

deformation between the fibers that are close to each other is larger than the other zones of matrix. It is assumed that the damage can also initiate from this location due to the local stress concentration. As the load increases, damage propagation along fiber–matrix interface (Fig. 4c) and fiber breakages at new locations are observed. At high relative flexural stress (95% σ_f), matrix microcracks occur at location where broken fibers are close to each other (Fig. 14a).

(b) RH = 50% specimen: Fig. 5a shows the surface of the specimen conditioned at RH = 50% subjected to a 30% σ_f. It can be seen that the damage is initiated in the form of interfacial debonding. However, it must be noticed that this damage initiation is not only observed at fiber ends but also at many locations where fibers are close to each other. The damage then propagates along the fiber–matrix interface, occurring both through the in-plane and out-of-plane directions, as shown in Fig. 5b. Some fiber breakages are evidenced at high relative flexural stress. However these fiber breakages are statistically small and hence cannot be considered predominant in terms of damage level. At high relative flexural stress (98% σ_f), matrix microcracks are observed (Figs. 5, 6, 7 and 14b). In addition, locally strained zone around fiber and cohesive fiber–matrix interface debonding are also evidenced, as shown in Figs. 6 and 7.

(c) RH = 100% specimen: Likewise to the RH = 50% specimen, the damage in RH = 100% specimen initiates at around 30% σ_f by fiber–matrix debonding at fiber ends and at locations where fibers are close to each other. Afterwards, the debonding propagates along the fiber–matrix interface. At high relative flexural stress, some fiber breakages are noticed. However, these fiber breakages cannot be considered predominant in terms of damage level as the number is statistically small. Matrix deformation bands and debonded fiber–matrix interfaces accompanied with locally strained zone around the fibers are also frequently observed at high relative flexural stress (98% σ_f), as shown in Figs. 8, 9 and 14c. Matrix deformation band is the zone where local matrix deformation is high. Compared to RH = 50% specimen, the RH = 100% specimen possesses significantly higher number of damaged area and higher occurrence of matrix microcracks and matrix deformation bands (Fig. 14c). The sequential images of the RH = 100% specimen from its initial state to the stress level right before the final failure which describes completely the whole chronology of damage mechanisms in RH = 100% specimen can be seen in Fig. 10.

4.2.2. Micro-computed tomography investigation and analysis of damage mechanisms

Damage mechanisms in PA66/GF30 composite with RH = 0% and 50% were assessed by µCT technique. The specimens were subjected to a tensile loading, which possesses the same loading as the outermost tensile region of the specimen under three-point bending load. As mentioned in Section 3.2, the µCT investigations were performed on samples extracted from the specimens that have been tensile loaded up to failure. These samples were extracted far from the fracture surface in order to focus the investigation in a damaged region and to avoid considering the localized failure zone. As shown in Figs. 11 and 12 obtained by µCT investigation of RH = 0% and 50% specimens, debonding at fiber ends and fiber sides, matrix microcracks and fiber breakages are observed. These findings confirm and strengthen the observations by in situ SEM test. The noticeable difference between RH = 0% and 50% specimens consists in the occurring of matrix microcracks. Indeed, while for RH = 0% specimen, the matrix microcracks exhibit brittle propagation, the ones in RH = 50% coalesce in ductile way. The

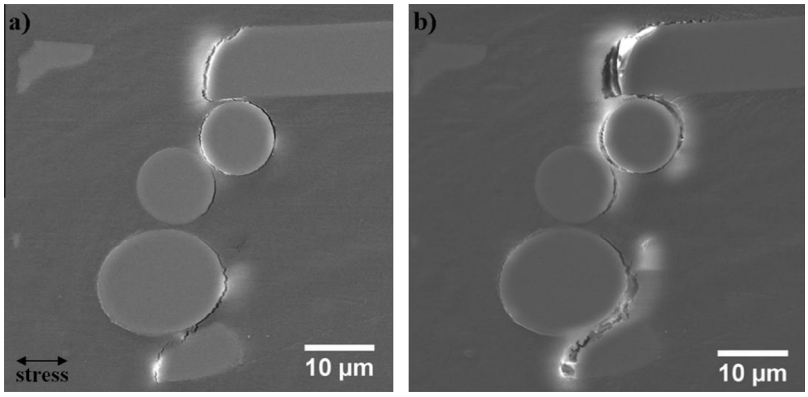

Fig. 5. PA66/GF30, RH = 50% specimen, (a) damage initiation at 30% σ_f and (b) damage propagation at 83% σ_f.

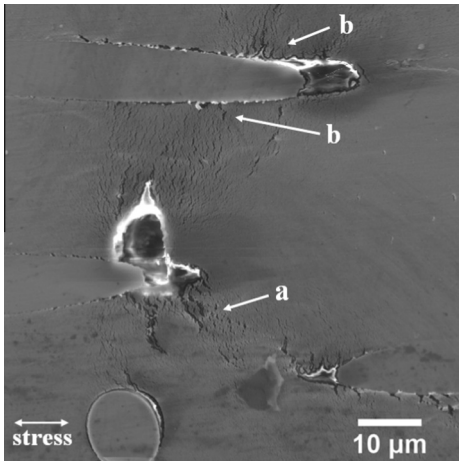

Fig. 6. PA66/GF30, RH = 50% specimen at 98% σ_f, (a) matrix microcracks and (b) locally strained zones around fiber.

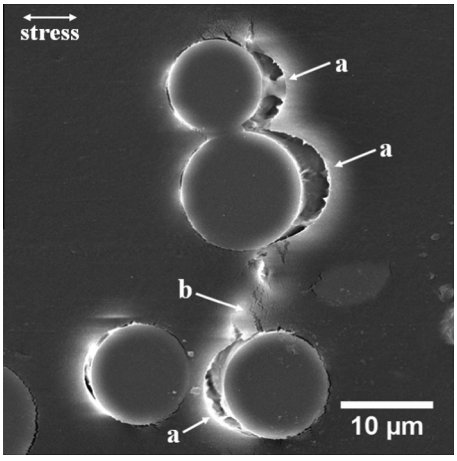

Fig. 7. PA66/GF30, RH = 50% specimen at 98% σ_f, (a) fiber–matrix interface debonding and (b) matrix microcracks.

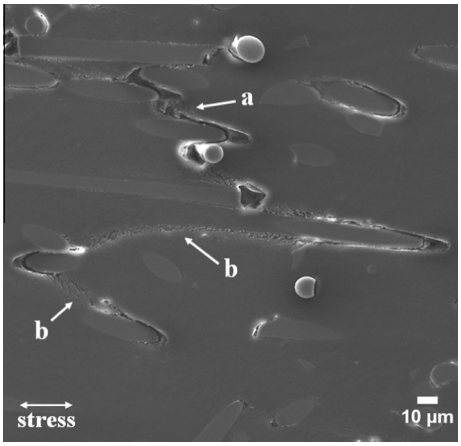

Fig. 8. PA66/GF30, RH = 100% specimen at 98% σ_f, (a) matrix microcracks and (b) matrix deformation band.

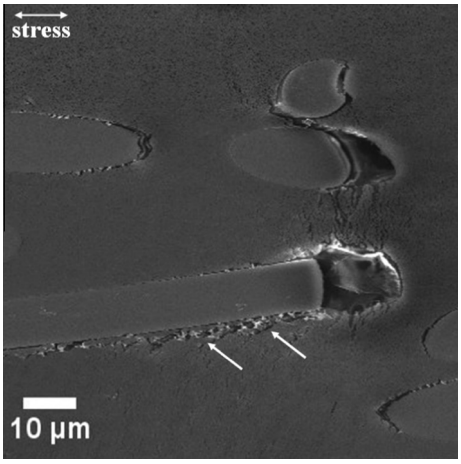

Fig. 9. Locally strained zone around fiber of PA66/GF30, RH = 100% specimen at 98% σ_f (indicated by arrow lines).

damage mechanisms found in the bulk material therefore correspond to the in situ SEM observations of the surface. This comparison confirms the validity of the in situ SEM observation technique described in this work to identify the damage mechanisms in PA66/GF30. The µCT observations at RH = 0% and 50% specimens are therefore considered sufficiently representative to complement the in situ SEM tests to investigate the damage mechanisms in dry and humid conditions.

For a purpose of qualitative comparison of these investigations with those on a virgin sample (non-tested), µCT observations have been performed on a non-tested sample extracted from an injected plate (as received). Fig. 13 performed at a resolution of 0.7 µm does

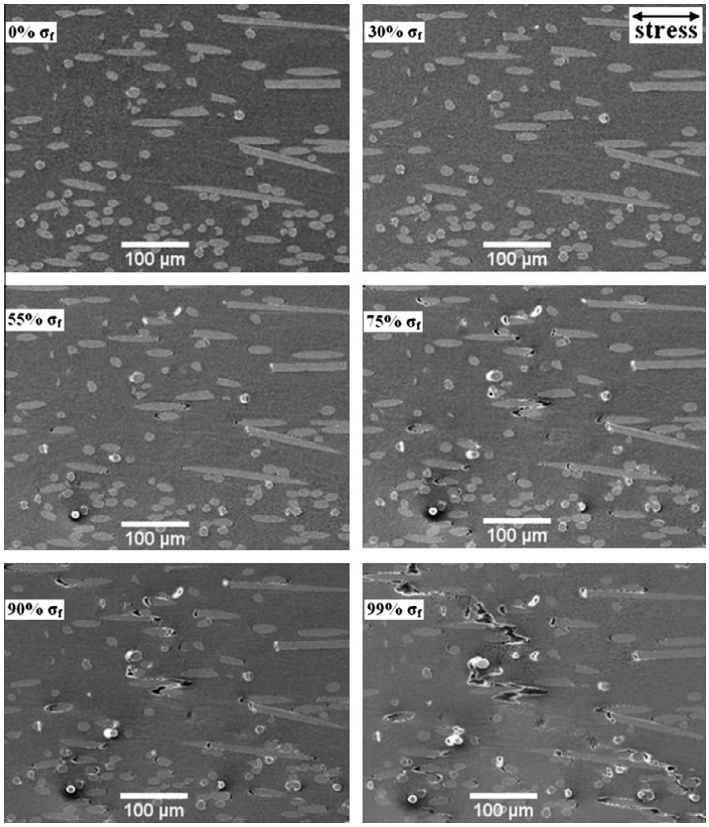

Fig. 10. SEM image sequences representing damage evolution of PA66/GF30, RH = 100% specimen from the virgin state to the stage prior to failure.

not show any noticeable damage for this non-tested sample. It confirms thus that the damage mechanisms evidenced on samples extracted from specimens loaded up to failure (Figs. 11 and 12) are induced by the applied stress. Consequently, they cannot be ascribed to a degradation induced by the injection process or to that induced by the machining during the µCT samples preparation.

5. Discussion

The damage mechanisms observed in PA66/GF30 are strongly affected by the moisture content variation. The flexural strength is reduced with increasing moisture content, which is assumed to be due to the combination of damage and polyamide plasticization effects (Fig. 2). Consistent results are also observed regarding to the qualitative observation of the number of damaged zone on the composites surface which shows that the higher RH results in higher damage level, at every stage of the loading. Moreover, Fig. 14 shows a comparison of damaged area for the three specimens with different moisture content at high relative flexural stress near to the failure. It is obvious that the number of damaged area increases while increasing the moisture content. The presence of water molecules inside the composite can reduce the mechanical performances of the polyamide as well as the fiber–matrix interfacial properties due to the plasticization effect and the mismatched fiber–matrix expansion during the ageing period. This might bring about a change in the overall mechanical and damage properties of PA66/GF30.

The damage initiation in the form of fiber–matrix debonding at fiber ends is observed and this experimental finding confirms the results reported by Sato et al. [9]. However, the interface debonding at fiber ends are not the only locations where the damage initiation exclusively occur. Indeed, the damage initiates also from

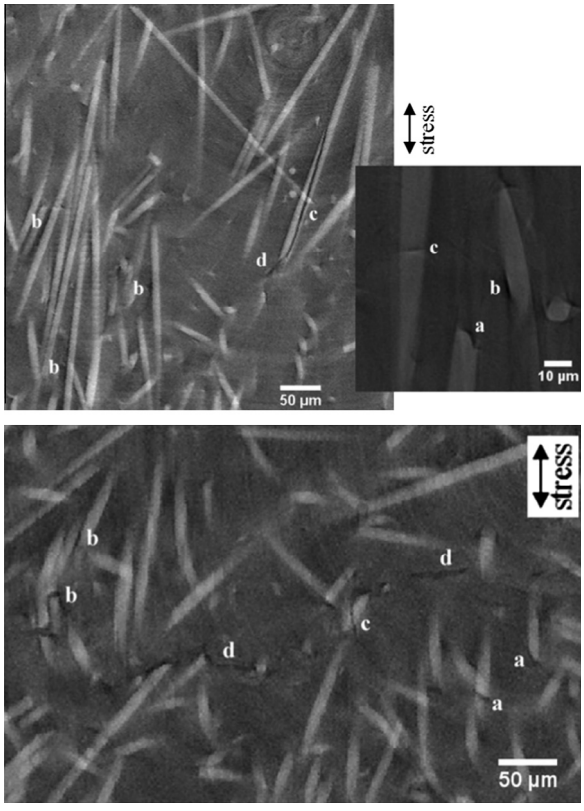

Fig. 11. Damage mechanisms observed by µCT in tensile specimen of PA66/GF30, RH = 0%: (a) debonding at fiber ends, (b) debonding at fiber–matrix interfaces, (c) fiber breakages and (d) matrix microcracks.

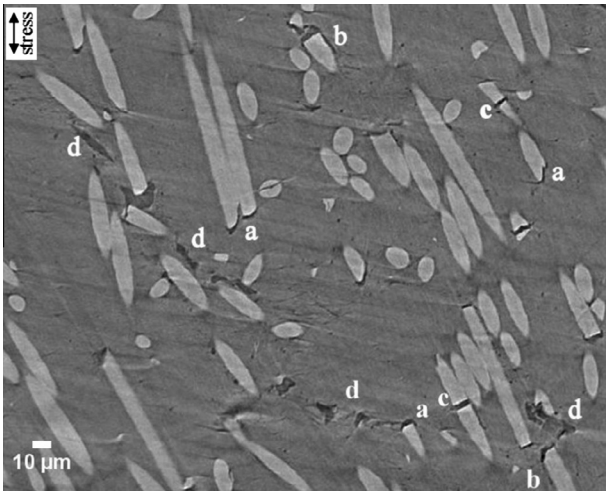

Fig. 12. Damage mechanisms observed by µCT in tensile specimen of PA66/GF30, RH = 50%: (a) debonding at fiber ends, (b) debonding at fiber–matrix interfaces, (c) fiber breakages and (d) matrix microcracks.

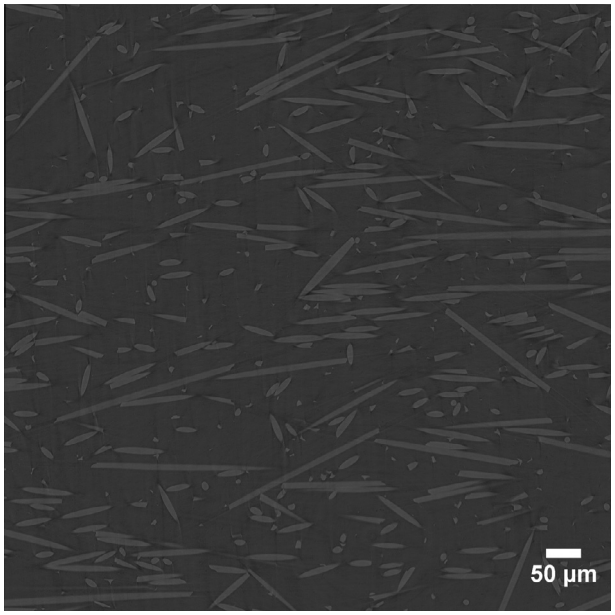

Fig. 13. An overview of µCT observation carried-out on a virgin sample (non-tested) extracted from an injected plate of PA66/GF30, RH = 0%. Noticeable damage, which can be induced by injection process or sample cutting preparation, is not observed.

locations where fibers are relatively close to each other. This mechanism has been observed in all investigated specimens regardless their RH contents. These local configurations generate stress concentrations, which induce an early occurrence of the damage. The damage initiations for RH = 0%, RH = 50% and RH = 100% specimens start around 30% of their respective flexural strength. If these relative percentages of flexural stresses are converted into the normalized load values based on the *y*-axes of Fig. 2, it can be seen that the damage initiations for RH = 0%, RH = 50% and RH = 100% respectively started at 0.33, 0.21 and 0.15 of normalized load values which shows that the damage in RH = 0% specimen starts to develop at significantly higher load level than those in RH = 50% and RH = 100% specimens.

For RH = 0% specimen where the water uptake is zero, the damage initiates at high load level and the damage remains confined and low. The damage has been notably observed in the form of fiber–matrix interfacial decohesions and fiber breakages (Fig. 4). This indicates that the RH = 0% specimen exhibits good interfacial properties compared to both other RH conditions. This is mainly due to the absence of water content and small level of interfacial decohesion while stress level increases. The good interfacial properties insure a stress distribution in the fibers when the composite is subjected to mechanical loading. This aspect increases the probability of occurring of fiber breakages and thus it is possible to observe few fiber breakages at the damage onset corresponding to 33% of σ_f. As this is only the damage initiation, the number of fiber breakages is very limited and confined in few locations of the investigated zone. This is common in short fiber reinforced composites due to their aspect ratios, local orientation with respect to the macroscopic applied stress and the local multi-axial stress concentration. At high relative flexural stress, matrix microcracks initiate at locations where broken fibers are close to each other (Fig. 14a). Fiber breakage induces stress redistribution into the matrix and surrounding fibers. Since locations where fibers are close to each other also generate local stress concentration, the matrix microcracks and another breakage of the adjacent fibers would occur. These matrix microcracks than propagate in a brittle way (Fig. 11).

The specimens with RH = 50% and RH = 100% exhibit many fiber–matrix interfacial decohesions, with localized strained matrix around the decohesion zones. The difference between both RH levels is the lower damage level of RH = 50% specimen than that of RH = 100% specimen (Fig. 14b and c). Matrix microcracks that preferably propagate in a ductile way are observed both in RH = 50% and 100% specimens. Matrix deformation bands, which indicate high local deformation of matrix are observed frequently in RH = 100% specimen (Figs. 8 and 14c). However, this occurrence is not dominant for RH = 50% specimen. It is noted that a high moisture induces a high plasticization effect, which could explain

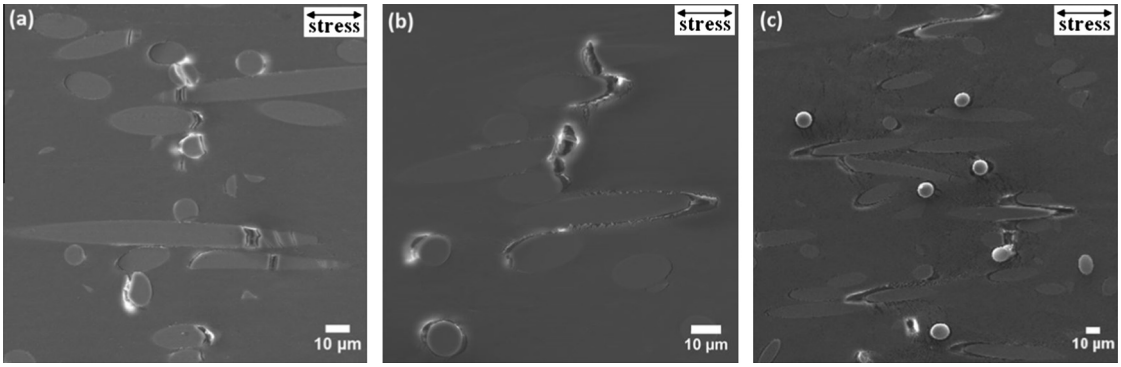

Fig. 14. Damage mechanisms of PA66/GF30 at different RH content, (a) fiber breakages and matrix microcracks at 95% σ_f of RH = 0%, (b) matrix microcracks at 98% σ_f of RH = 50%, (c) matrix microcracks and matrix deformation bands at 98% σ_f of RH = 100%.

the presence of localized deformation band in the RH = 100% specimen.

It is noted that some fiber breakages are observed on the specimens with RH = 50% and RH = 100% at high relative flexural stress level. These fiber breakages occur statistically in small proportions and hence induce a load transfer to the surrounding matrix leading to the matrix microcracks and interfacial debonding propagation. In addition, as abovementioned in this section, fiber–matrix decohesion happens at a stress level significantly lower than in the case of RH = 0%. This indicates that the interfacial properties are degraded when the moisture content is high due the water uptake of the material. The water content has an influence on the matrix and therefore on the interfacial properties of PA66/GF30, which induces higher level of fiber–matrix decohesion. Due to the important fiber–matrix debonding, the stress magnitude in the fibers remains low even under high relative flexural stress, which explains why fiber breakages appear in small proportions compared to matrix microcracks and interfacial debonding.

6. Concluding remarks

The damage scenarios for PA66/GF30 specimens conditioned into different relative humidity contents have been investigated. Experimental results show that the relative humidity conditions strongly impact the damage mechanisms in terms of their level and chronology. The damage in RH = 0% specimen initiates at significantly higher load level that those in RH = 50% and RH = 100% specimens. The higher relative humidity conditions also results in higher damage level. The predominant damage mechanisms for RH = 0% specimen are fiber–matrix debonding at fiber ends and fiber sides, fiber breakages and brittle matrix crack propagation. RH = 50% and 100% specimens exhibit almost the same predominant damage mechanisms, though damage level between both RH contents is essentially different. For both RH contents, the predominant damage mechanisms are fiber–matrix debonding at fiber ends and fiber sides, accompanied with locally strained matrix zone around the debonded fibers and ductile matrix microcracks. Matrix deformation bands are observed frequently in RH = 100% specimen but this occurrence is not dominant in RH = 50% specimen. Comparisons with μCT results indicate that the observations of in situ specimens at the surface matched suitably with that observed inside the specimen for dry and humid specimens.

Based on such observations, damage chronologies that include the effect of moisture content are proposed as follows:

(i) Damage initiation occurs in the form of fiber–matrix debonding at fiber ends and more generally at locations where fibers are relatively close to each other due to the generation of local stress concentration (for three studied RH contents). Specifically for RH = 0%, damage initiation can also occur through some fiber breakages besides the previous forms of mechanisms.
(ii) Interfacial decohesions further propagate along the fiber–matrix interface (for all studied RH contents) accompanied with locally strained zone around the fiber (for RH = 50% and 100%), and occurrence of new fiber breakages (for RH = 0%).
(iii) At high relative flexural stress, matrix microcracks develop and propagate in a brittle way (for RH = 0%) and in a ductile way (for RH = 50% and 100%), accompanied with high matrix deformation bands (for RH = 100%).
(iv) The propagation of the matrix microcracks brings about the damage accumulation leading to the total failure.

The current experimental findings on physical aspect of damage are of importance for identifying local damage criteria that would be implemented into a predictive micromechanical model [33,34]. To this end, development of multi-scale constitutive models that include the damage evolution should integrate fiber–matrix interface damage kinetic coupled with the viscous rheology of the polyamide matrix in relation with the PA66/GF30 microstructure. A particular attention has to be devoted to the impact of the moisture content on the overall mechanical properties of the matrix and to the properties of the fiber–matrix interface to be able to accurately predict the occurrence of damage in PA66/GF30 composites.

References

[1] Bergeret A, Ferry L, Ienny P. Influence of the fibre/matrix interface on ageing mechanisms of glass fibre reinforced thermoplastic composites (PA-6,6, PET, PBT) in a hygrothermal environment. Polym Degrad Stab 2009;94:1315–24.
[2] Bergeret A, Pires I, Foulc MP, Abadie B, Ferry L, Crespy A. The hygrothermal behaviour of glass-fibre-reinforced thermoplastic composites: a prediction of the composite lifetime. Polym Test 2001;20:753–63.
[3] Carrascal I, Casado JA, Polanco JA, Gutiérrez-Solana F. Absorption and diffusion of humidity in fiberglass-reinforced polyamide. Polym Compos 2005;26:580–6.
[4] Monson L, Braunwarth M, Extrand CW. Moisture absorption by various polyamides and their associated dimensional changes. J Appl Polym Sci 2008;107:355–63.
[5] Hassan A, Rahman NA, Yahya R. Moisture absorption effect on thermal, dynamic mechanical and mechanical properties of injection-molded short glass-fiber/polyamide 6,6 composites. Fibers Polym 2012;13:899–906.
[6] Jia N, Fraenkel HA, Kagan VA. Effects of moisture conditioning methods on mechanical properties of injection molded nylon 6. J Reinf Plast Compos 2004;23:729–37.
[7] Bradley WL, Grant TS. The effect of the moisture absorption on the interfacial strength of polymeric matrix composites. J Mater Sci 1995;30:5537–42.
[8] Gautier L, Mortaigne B, Bellenger V. Interface damage study of hydrothermally aged glass-fibre-reinforced polyester composites. Compos Sci Technol 1999;59:2329–37.
[9] Sato N, Kurauchi T, Sato S, Kamigaito O. Microfailure behaviour of randomly dispersed short fibre reinforced thermoplastic composites obtained by direct SEM observation. J Mater Sci 1991;26:3891–8.
[10] Horst JJ, Spoormaker JL. Mechanisms of fatigue in short glass fiber reinforced polyamide 6. Polym Eng Sci 1996;36:2718–26.
[11] Horst JJ, Spoormaker JL. Fatigue fracture mechanisms and fractography of short-glassfibre-reinforced polyamide 6. J Mater Sci 1997;32:3641–51.
[12] Barbouchi S, Bellenger V, Tcharkhtchi A, Castaing P, Jollivet T. Effect of water on the fatigue behaviour of a pa66/glass fibers composite material. J Mater Sci 2007;42:2181–8.
[13] Mouhmid B, Imad A, Benseddiq N, Benmedakhène S, Maazouz A. A study of the mechanical behaviour of a glass fibre reinforced polyamide 6,6: experimental investigation. Polym Test 2006;25:544–52.
[14] Babout L, Maire E, Buffière J-Y, Fougères R. Characterization by X-ray computed tomography of decohesion, porosity growth and coalescence in model metal matrix composites. Acta Mater 2001;49:2055–63.
[15] Chateau C, Gélébart L, Bornert M, Crépin J, Boller E, Sauder C, et al. In situ X-ray microtomography characterization of damage in SiCf/SiC minicomposites. Compos Sci Technol 2011;71:916–24.
[16] Maire E, Babout L, Buffiere J-Y, Fougeres R. Recent results on 3D characterisation of microstructure and damage of metal matrix composites and a metallic foam using X-ray tomography. Mater Sci Eng: A 2001;319–321:216–9.
[17] McCombe GP, Rouse J, Trask RS, Withers PJ, Bond IP. X-ray damage characterisation in self-healing fibre reinforced polymers. Compos Part A: Appl Sci Manuf 2012;43:613–20.
[18] Cosmi F, Bernasconi A. Micro-CT investigation on fatigue damage evolution in short fibre reinforced polymers. Compos Sci Technol 2013;79:70–6.
[19] Krause M, Hausherr J-M, Krenkel W. (Micro)-crack detection using local Radon transform. Mater Sci Eng: A 2010;527:7126–31.
[20] Withers PJ, Preuss M. Fatigue and damage in structural materials studied by X-ray tomography. Ann Rev Mater Res 2012;42:81–103.
[21] Nouri H, Meraghni F, Lory P. Fatigue damage model for injection-molded short glass fibre reinforced thermoplastics. Int J Fatigue 2009;31:934–42.
[22] Launay A, Maitournam MH, Marco Y, Raoult I, Szmytka F. Cyclic behaviour of short glass fibre reinforced polyamide: experimental study and constitutive equations. Int J Plast 2011;27:1267–93.
[23] Meraghni F, Nouri H, Bourgeois N, Czarnota C, Lory P. Parameters identification of fatigue damage model for short glass fiber reinforced polyamide (PA6-GF30) using digital image correlation. Procedia Eng 2011;10:2110–6.
[24] Nouri H, Czarnota C, Meraghni F. Experimental parameters identification of fatigue damage model for short glass fiber reinforced thermoplastics GFRP. In: Haddar M, Romdhane L, Louati J, Ben Amara A, editors. Design and Modeling of Mechanical Systems. Berlin, Heidelberg: Springer, Berlin, Heidelberg; 2013. p. 523–30.

[25] Kammoun S, Doghri I, Adam L, Robert G, Delannay L. First pseudo-grain failure model for inelastic composites with misaligned short fibers. Compos Part A: Appl Sci Manuf 2011;42:1892–902.
[26] Launay A, Marco Y, Maitournam MH, Raoult I. Modelling the influence of temperature and relative humidity on the time-dependent mechanical behaviour of a short glass fibre reinforced polyamide. Mech Mater 2013;56:1–10.
[27] Hassan A, Salleh NM, Yahya R, Sheikh MRK. Fiber length, thermal, mechanical, and dynamic mechanical properties of injection-molded glass-fiber/polyamide 6,6: plasticization effect. J Reinf Plast Compos 2011;30:488–98.
[28] Bernasconi A, Davoli P, Basile A, Filippi A. Effect of fibre orientation on the fatigue behaviour of a short glass fibre reinforced polyamide-6. Int J Fatigue 2007;29:199–208.
[29] Klimkeit B, Castagnet S, Nadot Y, El Habib A, Benoit G, Bergamo S, et al. Fatigue damage mechanisms in short fiber reinforced PBT + PET GF30. Mater Sci Eng: A 2011;528:1577–88.
[30] Mlekusch B. Fibre orientation in short-fibre-reinforced thermoplastics II. Quantitative measurements by image analysis. Compos Sci Technol 1999;59:547–60.
[31] ID19 ESRF. <www.esrf.eu/UsersAndScience/Experiments/Imaging/ID19>.
[32] Akay M. Moisture absorption and its influence on the tensile properties of glass-fibre reinforced polyamide 6,6. Polym Polym Compos 1994;2:349–54.
[33] Desrumaux F, Meraghni F, Benzeggagh M. Micromechanical modelling coupled to a reliability approach for damage evolution prediction in composite materials. Appl Compos Mater 2000;7:231–50.
[34] Jendli Z, Meraghni F, Fitoussi J, Baptiste D. Multi-scales modelling of dynamic behaviour for discontinuous fibre SMC composites. Compos Sci Technol 2009;69:97–103.